Northumbria
University
NEWCASTLE

MXene ($Ti_3C_2T_x$) and Carbon Nanotube Hybrid Supported Platinum Catalysts for the High Performance Oxygen Reduction Reaction in PEMFC

Chenxi Xu[a,*], Chanchan Fan[a], Xiaole Zhang[a], Haotian Chen[b], Xiaoteng Liu[c], Zhaoming Fu[b,*], Ranran Wang, Tao Hong[a], Jigui Cheng[a],

a School of Materials Science and Engineering, Hefei University of Technology, Hefei, Anhui, P.R. China, 230009

b School of Physics, Henan Normal University, Xinxiang, Henan, P.R. China, 453007

c Faculty of Engineering and Environment, Northumbria University, UK, NE1 8ST

* Corresponding Authors, E-mail: xuchenxi31@126.com, fuzm.phy@htu.edu.cn

Abstract: The metal–support interaction offers electronic, compositional, and geometric effects that could enhance the catalytic activity and stability. Herein, a high corrosion resistance and an excellent electrical conductivity MXene ($Ti_3C_2T_x$) hybrid with CNT composite material are developed as a support for Pt. Such a composite catalyst enhances durability and improved Oxygen reduction reaction (ORR) activity compared with the commercial Pt/C catalyst. The mass activity of Pt/CNT-MXene demonstrates a 3.4-fold than that of Pt/C. The ECSA of Pt/CNT-$Ti_3C_2T_x$ (1:1) catalysts shows only 6% dropping with respect to Pt/C of 27% after 2000 cycle potential sweeping. Furthermore, the Pt/CNT-$Ti_3C_2T_x$ (1:1) is used as cathode catalyst

for single cell and stack, and the maximum power density of stack reach 138W. The structure distortion of the Pt cluster induced by MXene is disadvantageous to the desorption of O atoms. This issue can be solved by adding CNT on MXene to stabilize the Pt cluster. These remarkable catalytic performances could be attributed to the synergistic effect between Pt and CNT-$Ti_3C_2T_x$.

Keywords: MXene; synergistic effect; composite catalytic support; oxygen reduction reaction; Proton exchange membrane fuel cells

Introduction

Proton exchange membrane fuel cells (PEMFCs) have been considered as a promising power source because their high energy densities and non-pollutant emissions during operation. Oxygen reduction reaction (ORR) in cathode has been considered as the rate-limiting step in electrochemistry scheme for PEMFCs. Carbon black supported platinum has been widely reported as the most efficient ORR catalyst. However, the scarcity and high cost of Pt are the major obstacles to the large-scale commercialization of PEMFCs [1-4]. Therefore, the amount of Pt reduction while keeping high catalytic activity or increase the catalytic activity with the same Pt loading is necessary for ORR [5, 6]. A typical catalyst includes catalytic particles and support [7-10]. Enormous attention has been paid to develop the catalytic particles, such as the morphologies or structures modification [11-13], transition metal employed to alloy with Pt [14-18] etc. Recently, the catalytic particles loaded on the two-dimensional (2D) materials substrates were reported as a useful way to increase the catalytic activity and stability, owing to the reactive metal–support interaction

offering electronic, geometric and compositional effects [1, 2, 19-25].

MXene in the formula $M_{n+1}X_nT_x$ been exfoliated via selective etching of the "A" element from MAX phases (where M is an early transition metal, A is a main group IIIA or IVA element, and X is a C and/or N, T represents a surface termination group such as –O, F and/or –OH) [26-28]. MXene has attracted tremendous attentions as catalyst supports due to its good electronic conductivity, high specific surface area, hydrophilic properties and etc. [3, 23, 29, 30]. In addition, the MXene surface's functional groups could facilitate the adsorption of metal particles by electrostatic interactions thus anchoring the active sites [23]. Zhang et al. reported Pt single atoms anchor on the MXene surface through covalent bonding to enhance the catalytic activity that the catalyst exhibits a low overpotentials of 30 mV to achieve 10 mA cm $^{-2}$ for HER [1]. After the accelerated durability tests, the Pt/MXene catalyst performance much better stability than the commercial Pt/C [2]. However, the catalysts based on 2D materials often result in restacking, which limits ion and electron transport in the electrode. The poor charge transfer performance while MXene surface with amount of functional groups may limit its application. Therefore, an effective strategy to prevent restacking of MXene nanosheets and enhance the ionic and electrical transport is value to realize.

Herein, we report a method for preparing MXene/CNT by self-assembly of negatively charged $Ti_3C_2T_x$ flakes and positively charged CNTs. A platinum nanoparticle catalyst supported on MXene/CNT exhibiting enhanced catalytic activity and stability. In particular, the Pt/MXene-CNT catalyst demonstrates a 3.4-fold increase in mass

activity compared to the commercial Pt/C catalyst. A population analysis from density functional theory (DFT) calculations suggests that which facilitates ORR.

Materials and Methods

Chemical and Reagents: Ti_3AlC_2 was purchased from Laizhou Kaiyi Ceramic Materials Co., Ltd. Sodium borohydride, isopropanol, chloroplatinic acid, Hexadecyltrimethylammonium chloride, Cetyltrimethylammonium bromide（CTAB）, Lithium fluoride and Hydrochloric acid were purchased from Sinopharm Chemical Reagent Co., Ltd. Carbon nanotube was purchased from Beijing Boyu Gaoke New Material Technology Co., Ltd. All chemicals are in AR grade and used as received.

Preparation of $Ti_3C_2T_x$ nanosheets: Etching and stripping of Ti_3AlC_2 was carried out according to the literature [30]. Briefly, hydrochloric acid (HCl) was diluted into 10ml 9M HCl, and 0.8g LiF was injected to the diluted solution. The above solution was stirred at 20℃ for 5 min, and then 0.5g Ti_3AlC_2 was stepwise added with 24h further stirring at 35℃ to achieve $Ti_3C_2T_x$. The acidic mixture was washed with deionized water via centrifugation (5 min per cycle at 3500 rpm) for several times until the pH was about 7. $Ti_3C_2T_x$ was sonicated for another 1h. Finally, the supernatant was filtered by a porous MF-millipore mixed cellulose ester membrane filter (0.22 μm pore size) and dried at 30 ℃ in vacuum oven.

Preparation of Pt/CNT-$Ti_3C_2T_x$ catalyst: CTAB was dissolved in deionized water followed by adding CNT added, and the solution was ultrasonically dispersed for 1h at 20℃ to prepare CTAB-grafted CNT [30, 31]. Porous $Ti_3C_2T_x$/CNT composite

support was prepared by a self-assembly process. Typically, the CTAB-grafted CNT solution was added dropwise to $Ti_3C_2T_x$ suspension (The mass ratio of CNTs and $Ti_3C_2T_x$ was 1:1 and 2:1). Chloroplatinic acid ($H_2PtCl_6 \cdot 6H_2O$) and reducing agent (sodium borohydride) was added dropwise with ultrasonic. The precipitate Pt/CNT-$Ti_3C_2T_x$ was rinsed with ethanol and deionized water for five times and dried at 80 ℃ for 24hrs as shown in Scheme S1.

Materials Characterization: The crystal structure was examined using X-ray diffraction (XRD, PANalytical X'Pert Pro Diffractometer), with a 2θ range of 5~70°. The morphologies of materials were measured by a JSM-5300LV (Japan) Scanning Electron Microscope (SEM). X-ray Photoelectron Spectroscopy was conducted on ESCALAB250Xi spectrometer equipped with a monochromatic Al X-ray source (Al Kα, 14.8KV×9.5mA). High-resolution transmission electron microscopy (HRTEM) were conducted on a JEM-2100F instrument operating at 120 kV.

Electrochemical tests: The cyclic voltammetry (CV) and linear sweep voltammetry (LSV) were used to characterize the electrochemical performance of the catalyst. The test was carried out in a three-electrode system: the counter electrode is graphite rod, the reference electrode was an Ag/AgCl (saturated KCl), and the working electrode (WE) substrate was a glassy carbon electrode. Pt/CNT-$Ti_3C_2T_x$ (1:1), Pt/CNT-$Ti_3C_2T_x$ (2:1), Pt/CNT-$Ti_3C_2T_x$ (1:2) and Pt/C were dissolved in solution (500ul deionized water: 450ul isopropanol: 50ul 5wt.% Nafion solution). All the electrochemical experiments were performed in 0.1 M $HClO_4$ using Autolab PGSTAT302. In this study, all potentials values were given vs the reversible hydrogen electrode (RHE) if

not specified. A rotating disk electrode (RDE) with a glassy carbon (0.1963 cm^2) was used as the working electrode. The electrochemical surface areas (ECSA) were calculated by the following equation:

$$\mathrm{ECSA} = \frac{S_H/v}{0.21(mC\ cm^{-2})M_{Pt}} \quad (1)$$

where S_H is the hydrogen desorption peak or the integrated area of the hydrogen adsorption peak of the CVs, v is the scanning speed, M_{Pt} is the loading of Pt on the working electrode.

Oxygen reduction reactions were conducted in a 0.1 M $HClO_4$ aqueous solution. The polarization curves were obtained at a scan rate of 10 mV s^{-1} and a rotation rate of 1600 rpm by sweeping the potential from 1.2 to 0.2 V. The current density was normalized in reference to the ECSA of the catalyst. Based on the ORR polarization curves, the number of electrons transferred (n) during the course of the ORR was calculated from the slopes of Koutecky-Levich (K-L) plots using the following equation:

$$\frac{1}{J} = \frac{1}{J_K} + \frac{1}{J_D} = \frac{1}{J_K} + \frac{1}{B\omega^{1/2}} \quad (2)$$

$$\mathrm{B} = 0.2\mathrm{nFC}D^{2/3}v^{-1/6} \quad (3)$$

Where J is the measured current density, J_K and J_D are the kinetic and diffusion-limiting current densities, n represents the electron transfer number, F is the Faraday constant, D is the diffusion coefficient, v is the kinetic viscosity and C is the bulk concentration of O_2.

Fuel cell performance test: The catalysts was dispersed in a water/isopropanol

mixture with ultrasonic vibration to achieve the ink. The size of the gas diffusion layer (carbon paper, Avcarb GDS2240) was 1cm^2. The Pt loadings on the electrode were both 0.2 mg cm^{-2}. The (Membrane electrode assembly) MEA was obtained by pressing the electrodes onto Nafion 211 membranes for 2 min at 130^{o}C. H_2 and air were fed into the cell at flow rates both of 150 cm^3 min^{-1}. The stability of cell was tested at 0.3V for 6h. The catalysts used for the cathode and anode of the fuel cell are 20wt.% Pt loaded catalysts, the carbon paper used contains microporous layer and keeps humidifying during the test. The fuel cell stack with 22 MEAs (10 wt. % Pt/ CNT-$Ti_3C_2T_x$ (1:1) and 90 wt. % Pt/C mixture catalyst for cathode) was test under H_2/air at 25℃.

Computational Section: Methods and Models. First-principle calculations are performed using the Vienna Ab initio Simulation Package (VASP) code [32,33] with the Perdew–Burke–Ernzerhof functional [20] and projector-augmented wave (PAW) potential [34,35]. The Van der Waals (vdW) interactions are considered using the DFT-D3 method [36]. The transition states are calculated by CI-NEB method [37]. The models of $Ti_3C_2T_x$-suported Pt cluster with and without CNT are simulated (see Fig. S5(a) and (b)). Here, the group T_x on Ti_3C_2 is considered only by adding hydroxy OH^-, and the armchair CNT (7,7) are constructed yielding the tube diameter of 9.55 Å. We cleave two atomic layers along Pt <111> direction to simulate the supported Pt cluster. Pt cluster and CNT remain a periodic structure along ***a*** axis in our models. To this purpose, a very large supercell is needed to reduce the lattice mismatch. The models with and without CNT include 312 and 200 atoms respectively. The lattice

mismatch is less than 5% in these two models. Considering the large diameter (9.55 Å) of CNT, the thickness of vacuum layer is set to be sufficiently large (25 Å) between two MXene layers belonging to two supercells respectively, to eliminate supercell-supercell interactions perpendicular to the surface.

Results and Discussions

Preparation and characterizations of the Pt/CNT-$Ti_3C_2T_x$. The preparation of few-layer $Ti_3C_2T_x$ is summarized in the Methods. The X-ray diffraction (XRD) patterns in Fig. S1a shows that the characteristic peaks of $Ti_3C_2T_x$. The (002) peak of $Ti_3C_2T_x$ powder shifted to 2θ of 7.2°, which corresponds to a interlayer space of 1.23 nm different from that in the initial MAX (Ti_3AlC_2) phase (9.6°). The dominant peak of $Ti_3C_2T_x$ is left shifted to 6.2° after ultrasonic stripping. Furthermore, the XRD pattern of Pt/CNT-$Ti_3C_2T_x$ exhibits the characteristic peak of CNT at 25.9° and Pt (111) and (200) at 39.8° and 46.3°, respectively. Similarly, the Raman spectra in Fig. S1b reveal the six different vibration modes (A(209 cm^{-1}), B(270 cm^{-1}), C(383 cm^{-1}), D(591 cm^{-1}), E(629 cm^{-1}) and F(734 cm^{-1})) of $Ti_3C_2T_x$ comparing to MAX-Ti_3AlC_2 (a(128 cm^{-1}), b(185 cm^{-1}), c(205 cm^{-1}), d(274 cm^{-1}), e(488 cm^{-1}) and f(653 cm^{-1})) corresponding to the vibration response of $Ti_3C_2T_x$ (T_x=O_2, $(OH)_2$, O(OH) and F_2) for Ti2, C, O and F atoms, respectively, further proving the exfoliation process [38].

The X-ray photoelectron spectroscopy (XPS) survey scan results showed that the content of Al (74.83ev) decreased after etching and ultrasonic stripping (Fig. S2a-c). An amount of –OH and/or –F groups introduced during the HF etching process

actives as anchor points that may facilitate the dispersion and binding for Pt nanoparticles on MXene [2]. Moreover, the Pt $4f_{5/2}$ binding energy of Pt/CNT-$Ti_3C_2T_x$ is 71.16 eV, which shifts 0.21 eV to higher value compared to Pt/C (71.37 eV; Fig S2d). This indicates the stronger interaction between the CNT-$Ti_3C_2T_x$ support and Pt nanoparticles than that of carbon and Pt [3]. The peaks of Pt $4f_{7/2}$ and Pt $4f_{5/2}$ correspond to two peaks: Pt^0 and Pt^{2+}, respectively (Fig S3 and table S1), This indicates the formation of the oxidized Pt species.

TEM and HRTEM images in Fig.1a, b shows that the exfoliated CNT-$Ti_3C_2T_x$ nanosheets consist of only a few layers of $Ti_3C_2T_x$ and the Pt particle size distribution. The layered $Ti_3C_2T_x$ with negative charge and CTAB modified CNT with positive charge are self-assembly of the hybrid support CNT-$Ti_3C_2T_x$. The Pt particles are dispersed uniformly on the CNT-$Ti_3C_2T_x$ support with a size distribution around 2-5 nm. The distance of Pt particle between two lattice planes is around 0.23 nm, which can be recognized to Pt (111) in Pt/CNT-$Ti_3C_2T_x$ as Fig. 1c, d shown. Fig. 1c, d images of Pt show their multi crystalline structure with a highly ordered continuous fringe pattern, and most of the exposed facets were found to be (111), although a small fraction of (110) and (100) facets could also be identified. Bright spots are observed in HAADF–STEM image in Fig. 1e, which confirms the formation of Pt atoms on the CNT-$Ti_3C_2T_x$ nanosheets. The EDS mapping of the Pt/CNT-$Ti_3C_2T_x$ catalyst shows that the characteristic elements Ti, F and O of $Ti_3C_2T_x$ and the N element of CTAB are evenly distributed, indicating that Pt particles have good dispersibility on the ultra-thin CNT-$Ti_3C_2T_x$ support.

.

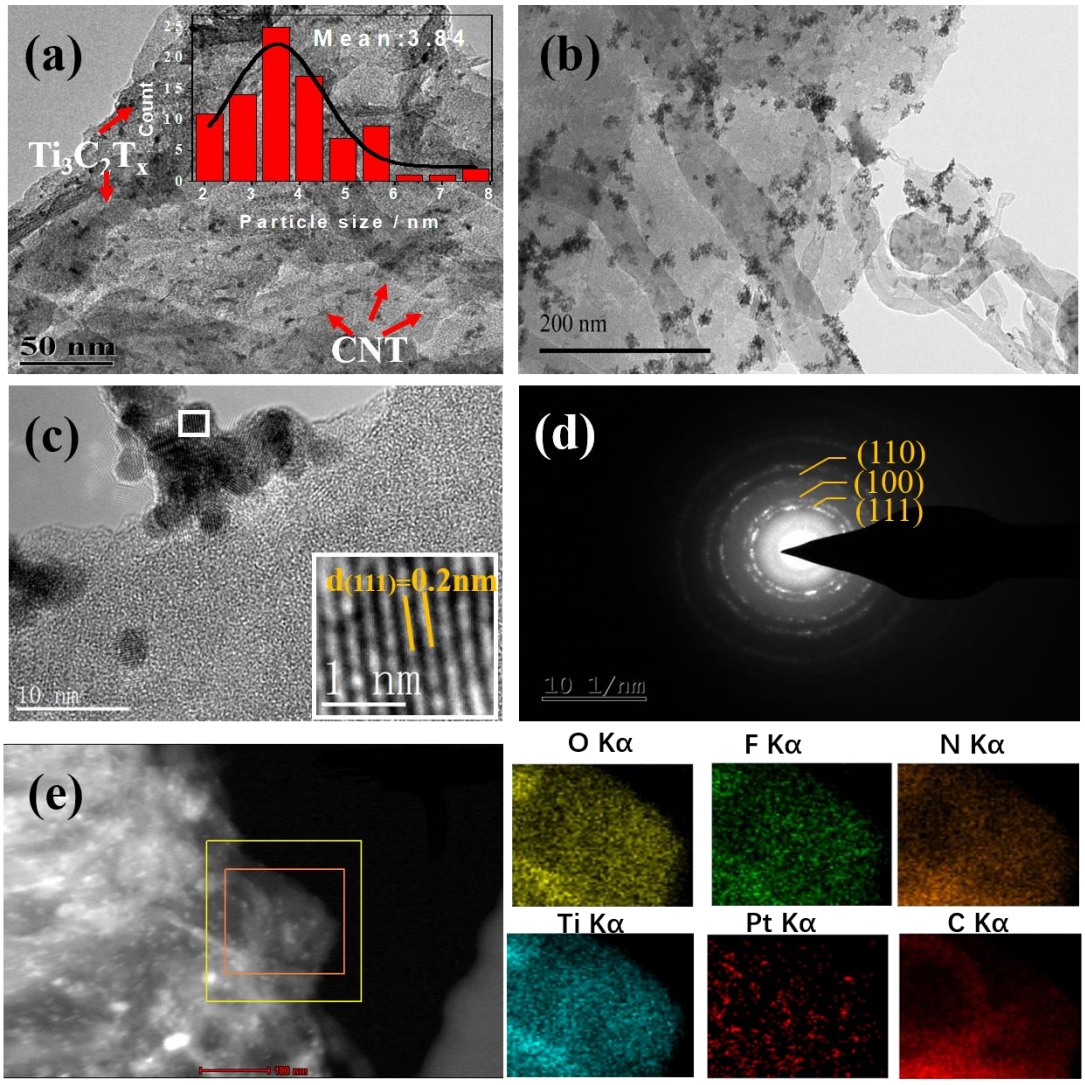

Figure 1, (a) TEM image and Particle size distribution of Pt/CNT-$Ti_3C_2T_x$ catalyst, (b) and (c) HRTEM image of Pt/CNT-$Ti_3C_2T_x$ catalyst, (d) SAED image of Pt particles, (e) The HAADF-STEM image and EDS mapping of Pt/CNT-$Ti_3C_2T_x$ catalyst

Electrochemical ORR evaluation of Pt/CNT-$Ti_3C_2T_x$. The ORR activity of the Pt/CNT-$Ti_3C_2T_x$ was evaluated with the graphite rod as the counter electrode in $HClO_4$ solution. Fig. 2a exhibits CV curves revealing a discernible positive shift in the peak potential of the reduction of OH groups adsorbed on the Pt/CNT-$Ti_3C_2T_x$

catalyst surfaces compared with that corresponding to the Pt/C surface. This indicates that Pt/CNT-$Ti_3C_2T_x$ has more active sites for ORR because of a lower OH chemisorption energy [3, 39]. The half-wave potential of Pt/CNT-$Ti_3C_2T_x$ (1:1, 0.876V) exhibits a positive right shift of approximately 41 mV, 31mV, 29 mV, 24mV and 65mV relative to that of Pt/C (0.835V), Pt/CNT-$Ti_3C_2T_x$ (2:1, 0.845V), Pt/CNT-$Ti_3C_2T_x$ (1:2, 0.847V), Pt/$Ti_3C_2T_x$ (0.852V) and Pt/CNT (0.811V) shown in Fig. 2b. It reveals the substantial ORR activity at lower over-potentials. The specific and mass activities of Pt-based ORR electrocatalysts at 0.9V have been widely used to evaluate their electro-catalytic activities. The electrochemical surface areas (ECSAs) of Pt/C, Pt/CNT-$Ti_3C_2T_x$ (1:2), Pt/CNT-$Ti_3C_2T_x$ (2:1), Pt/CNT-$Ti_3C_2T_x$ (1:1), Pt/$Ti_3C_2T_x$ and Pt/CNT catalysts are calculated as 46.7 $m^2\ g^{-1}$, 57.4 $m^2\ g^{-1}$, 34.2 $m^2\ g^{-1}$, 63.0 $m^2\ g^{-1}$, 19.9 $m^2\ g^{-1}$ and 34.9 $m^2\ g^{-1}$, respectively. Moreover, their specific activities are 0.103 mA cm^{-2}, 0.207 mA cm^{-2}, 0.147mA cm^{-2}, 0.259 mA cm^{-2}, 0.0849 mA cm^{-2} and 0.0229 mA cm^{-2}, respectively. Similarly, after normalization to the loading amount of Pt metal (1.8μg), the mass activity of the Pt/CNT-$Ti_3C_2T_x$ (1:1, 0.163 A mg^{-1}), Pt/ CNT-$Ti_3C_2T_x$ (2:1, 0.0504 A mg^{-1}) and Pt/CNT-$Ti_3C_2T_x$ (1:2, 0.117 A mg^{-1}) are 3.4, 1.05 and 2.4 times than that of Pt/C (0.048 A mg^{-1}), respectively. The limiting current density (LCD) of Pt/CNT-$Ti_3C_2T_x$ (1:1), Pt/CNT- $Ti_3C_2T_x$ (1:2) and Pt/CNT-$Ti_3C_2T_x$ (2:1) increased with rotational speed increasing because of the more O_2 diffusing to the electrode surface as shown in Fig. S4a, b, c. The LSV (Fig. 2d) of Pt/CNT-$Ti_3C_2T_x$ (1:1) showed good linearity and near parallelism of the fitting lines, indicating the first order kinetics with respect to dissolved O_2 and similar electron

transfer numbers for ORR at different potentials. From the slope of the K-L curve, the number of electron transfers (n) of Pt/CNT-$Ti_3C_2T_x$ (1: 1) was 3.7, which was consistent with the theoretical four-electron transfer.

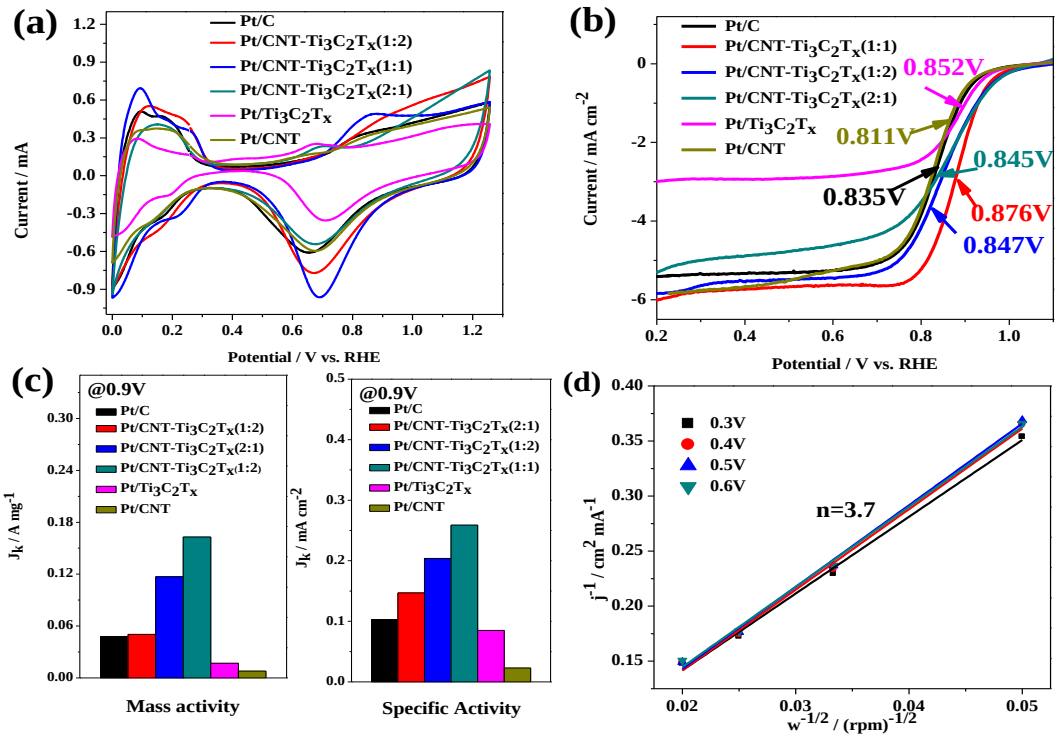

Figure. 2, (a) CV curves for Pt/CNT-$Ti_3C_2T_x$, Pt/$Ti_3C_2T_x$, Pt/C and Pt/CNT catalysts (recorded in 0.1M N_2-saturated $HClO_4$ with a scan rate of 50 mV/s). (b) ORR polarization curves for Pt/CNT-$Ti_3C_2T_x$, Pt/$Ti_3C_2T_x$, Pt/C and Pt/CNT catalysts (recorded in O_2-saturated 0.1M $HClO_4$ at 1600rpm and with a scan rate of 10 mV/s). (c) Specific activity and mass activity at 0.9 V for Pt/CNT-$Ti_3C_2T_x$, Pt/$Ti_3C_2T_x$, Pt/C and Pt/CNT catalysts. (d) Corresponding Koutecky–Levich plots of Pt/CNT-$Ti_3C_2T_x$ (1:1) at different potentials.

Pt/CNT-$Ti_3C_2T_x$ (1:1) demonstrated a better electrocatalytic stability compared with

Pt/C under the same Pt loading (1.8 μg) as shown in fig 3a. The ECSA of Pt/CNT-$Ti_3C_2T_x$ (1:1) catalysts maintained at the equal value of 60 m^2 g^{-1}, which is only 6% dropping with respect to Pt/C of 27% after 2000 cycles potential sweeping (Fig. 3b). Thus, Pt/CNT-$Ti_3C_2T_x$ (1:1) exhibits a 4.5-fold improvement. Fig. 3c, d exhibit the half-wave potential of Pt/CNT-$Ti_3C_2T_x$ (1:1) catalysts had dropped by 19mV while Pt/C lost 23 mV. The TEM image confirms that Pt particles of Pt/CNT-$Ti_3C_2T_x$ (1:1) catalyst have no noticeable aggregation after the 2000 cycles potential sweeping. Therefore, the Pt/CNT-$Ti_3C_2T_x$ (1:1) catalyst is more electrochemically stable than the Pt/C catalyst. The existence of CNT could introduce space vectors between the $Ti_3C_2T_x$ flakes, which can effectively prevent the $Ti_3C_2T_x$ re-stacking. Moreover, the CNT could reduce the deformation of Pt clusters while $Ti_3C_2T_x$ flakes could serve as arching site to provide strong adsorption to Pt.

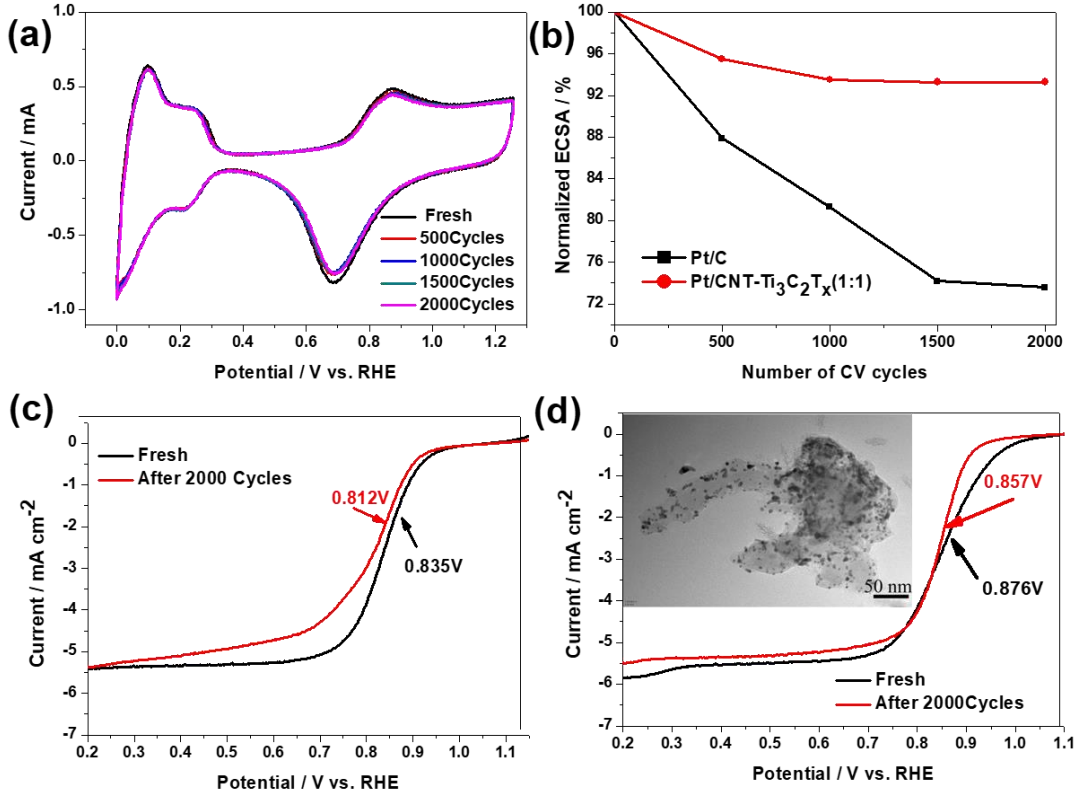

Figure. 3, CV curves for (a) Pt/CNT-$Ti_3C_2T_x$(1:1) catalysts (recorded in 0.1M N_2-saturated $HClO_4$ with a scan rate of 100 mV s^{-1}); (b) Normalized Pt ECSA of Pt/CNT-$Ti_3C_2T_x$(1:1) and Pt/C catalysts as a function of the number of CV cycles; ORR polarization curves for (c) Pt/C; (d) Pt/CNT-$Ti_3C_2T_x$ (1:1) catalysts before and after the accelerated durability tests cycling (recorded in O_2-saturated 0.1M $HClO_4$ at 1600 rpm and with a scan rate of 10 mV s^{-1}), the insert image shows the TEM of Pt/CNT-$Ti_3C_2T_x$ (1:1) catalysts after 2000 cycles.

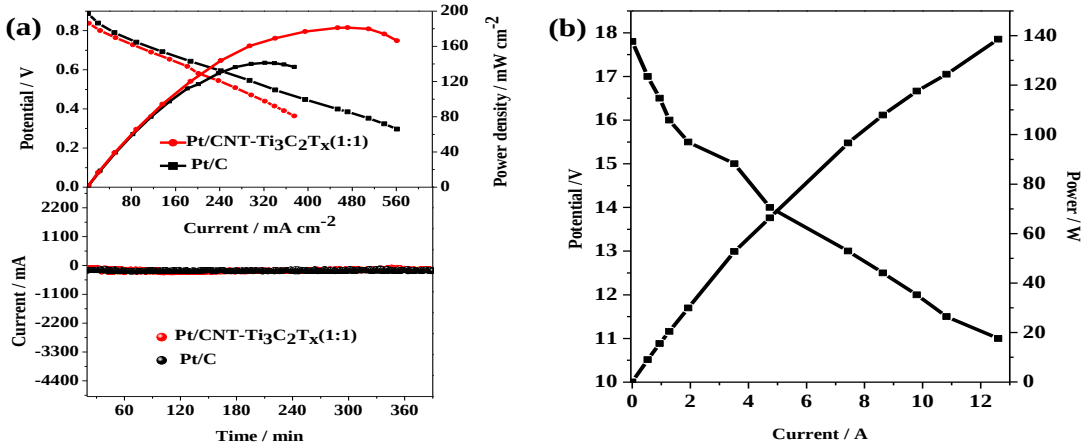

Figure 4, Polarisation and power density、stability curves (a) of Pt/CNT-$Ti_3C_2T_x$(1:1) and Pt/C catalysts used in H_2/air fuel cells operated at 60℃; (b) Fuel cell stacks performance in H_2/air at 25℃

In order to evaluate the Pt/CNT-$Ti_3C_2T_x$ (1:1) catalyst under PEMFC operating conditions, they were integrated as cathodes into a single cell MEA working at 60°C and atmospheric pressure as shown in Fig. 4 (a). MEAs consisted of Pt/CNT-$Ti_3C_2T_x$ (1:1) (0.2 $mg_{Pt}\,cm^{-2}$) as cathode catalyst for ORR, and Pt/C (0.2 $mg_{Pt}\,cm^{-2}$) as anode catalyst for H_2 oxidation. H_2–Air performance provides practical operative conditions. For comparison, the fuel cell curve with commercial Pt/C catalyst at cathode was also obtained under identical conditions. The anode using commercial Pt/C catalyst was set as standard. Activation over-potential losses which manifest in the polarization curves at lower current density region (normally <100 mA cm^{-2}), arise predominantly because of the slower kinetics of the reaction at the cathode. The higher cell voltage value with Pt/CNT-$Ti_3C_2T_x$ (1:1) catalyst implies lower activation over-potential loss and better ORR catalytic activity that could be attributed to stronger metal-support interaction and faster interfacial oxygen kinetics [40]. Moreover, the fuel cell

performance with Pt/CNT-$Ti_3C_2T_x$ (1:1) is close to that using Pt/C as cathode catalyst at the current density below 300 mA cm^{-2}. However, the Pt/CNT-$Ti_3C_2T_x$ (1:1) exhibits a performance better than the Pt/C owing to fast mass transfer of the Pt/CNT-$Ti_3C_2T_x$ (1:1) catalyst at the concentration polarization region [41]. The peak power density of Pt/CNT-$Ti_3C_2T_x$ (1:1) and Pt/C catalyst used in fuel cells are 181 mW cm^{-2} and 141 mW cm^{-2}, respectively. PEMFC with Pt/C and Pt/CNT-$Ti_3C_2T_x$ (1:1) catalysts were operated at 0.30 V for 360 min. The current densities of both cell keep a straight line without obvious decline indicating a similar durability of these two catalyst. The above results demonstrate the superior performance of CNT-$Ti_3C_2T_x$ (1:1) supported Pt catalyst as an ORR catalyst for fuel cell. The Pt/CNT-$Ti_3C_2T_x$ (1:1) was mixed with Pt/C as catalyst to evaluate the performance for the practical application as shown in Fig. 4(b). However, only 10 wt.% Pt/CNT-$Ti_3C_2T_x$ (1:1) was used in catalyst because of large amount catalyst required for the fuel cell stack. The Open circle voltage (OCV) of 18V is achieved. The PEMFC stack delivers cell voltage of 12V at a current density of 8.3 A at 25℃. The maximum power density of stack is 138.6 W at 11V and 12.6A. The results further confirm the enhanced catalytic performance of Pt/CNT-$Ti_3C_2T_x$ (1:1) for the PEMFC.

The aforementioned electrochemical tests indicate CNT-modified MXene substrate (CNT-MXene) can significantly enhance the catalytic activities of Pt clusters. To clarify the intrinsic relationship between the surface composition of Pt/CNT-$Ti_3C_2T_x$ in an acidic solution, we performed first-principles simulations to explore the the mechanism of cooperative activation effects on electrochemical reaction in

CNT-modified cathode. Fig. S5(a) and (b) show the Pt clusters on MXene with and without CNT-modification, denoted by Pt/MXene and Pt/CNT-MXene respectively (see method and Supplementary Fig S5-6 for details).

The adsorption and dissociation of O_2 molecules, as well as the desorption of O atoms on two kinds of catalyst are calculated, which are described by the adsorption energy (E_{ad}) of O_2, dissociation barrier (E_{bar}) of O_2, and binding energy (E_{bind}) between O atoms and Pt catalysts, respectively. The definitions are given by the following equations:

$$E_{ad} = E(\text{catalyst}) + E(O_2) - E(O_2/\text{catalyst}) \quad (4)$$

$$E_{bar} = E(\text{transition state}) - E(\text{initial state}) \quad (5)$$

$$E_{bind} = E(\text{catalyst}) + 0.5*E(O_2) - E(O/\text{catalyst}) \quad (6)$$

To accelerate electrochemical reaction rate on cathodes, the E_{ad} of O_2 should be enhanced by cathodic catalysts. Simultaneously, both E_{bind} of O and E_{dis} of O_2 should be reduced. Table S3 suggests that, on both two kinds of cathodes, O_2 molecules have the small dissociation barriers of about 0.366 eV (Fig. S6), significantly smaller than that on Pt (111) surface (0.52~0.72 eV), a typical ORR catalyst [42]. These results of E_{bar} suggest that, two kinds of cathodes both improve the O_2 dissociation compared to Pt (111) surface on the one hand; and CNT-modification has a less impact on the O_2 dissociation compared to the cathode without CNT on the other hand. For O_2 adsorption, the effect of CNT on adsorption strength is also small according to the calculated E_{ad}. The calculated projected density of states (DOS) of the *d*-electrons is given in Fig. 5(a) for Pt on MXene and CNT-MXene substrates. Compared with the

projected DOSs on these two substrates, it is found that the positions of the projected DOS peak have no obvious changes relative to the Fermi level (see the red arrow in Fig. 5(a)), which could be responsible for the similar adsorption and dissociation activities of O_2 on two kinds of cathodes.

Many recent works point out that the desorption of O atoms could be a vital step on cathode catalysts by binding H^- to form H_2O. The high O binding energy would result in a slow step of further reduction of adsorbed oxygen adsorbates [43, 44]. Our calculated E_{bind} suggest that, on Pt/CNT-MXene, the desorption of O atom obviously become much easier than that on the cathode without CNT (See Table S3). The E_{bind} on Pt/CNT-MXene and Pt/MXene are 0.337 and 0.683 eV respectively. Therefore, CNT-modification is obviously advantageous to improve the ORR activity of cathodes. An interesting issue is how CNT-modifications weaken the binding of O atoms on Pt cluster. To answer it, the effects of CNT-modifications on the geometric structures of Pt clusters are taken into account and given in Fig. 5(b). It is found that there exists a remarkable structure distortion of the Pt cluster without CNT-modifications, corresponding to a bad stability of Pt cluster on MXene. In contrast, on CNT-MXene substrates no large distortion is observed for the Pt cluster (see Fig. 5(b)). Therefore the CNTs could contribute to improving the stability of Pt cluster. Based on this, the larger binding energy of O atom on Pt/MXene would mainly originate from the strong bonds between O atoms and local Pt atoms at distortion regions. These theoretical results discover the mechanism that CNTs improve the electrochemical performance of cathodes. For the O_2 dissociation and

adsorption, the charge transfer play a major role from Pt *d*-electrons into the antibonding π* orbital of adsorbed O_2 molecules, so the effects of electronic structures are dominant. On two kinds of substrates, the similarity of the *d*-electron DOS near Fermi level would lead to the similar E_{ad} and E_{bar} of O_2 molecules. For the bonding of the single O atom on Pt surface, the 2*p*-orbitals of the O atom will hybridize with Pt atoms, i.e., the local active Pt atoms on distorted surface would have a significant impact on the E_{bind} of single O atom. Correspondingly, the geometric structures and stabilities of the Pt cluster become important for binding O atoms. Additionally, we also discussed the reason why MXene-supported Pt has relative high activities for O_2 dissociation compared with Pt(111) surface. The detailed results are given in Fig. S8. The calculated results are shown in the following figure, in which we use the same number of Pt atoms to calculate the PDOS. Obviously, the PDOS of MXene-supported Pt have higher peaks near the Fermi level than that of Pt(111) surface, which should be responsible for the higher activities, corresponding to a lower E_{bar} for O_2 dissociation.

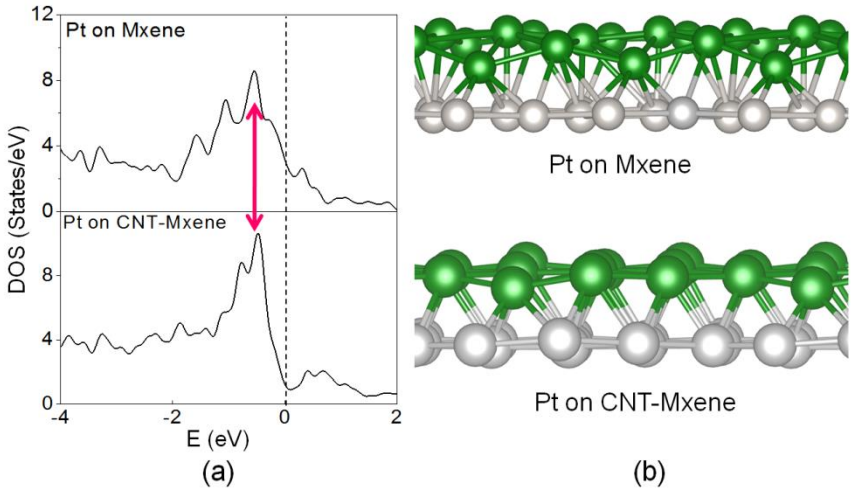

Figure 5, (a) Projected DOS of d-electrons of surface Pt atoms on MXene (above)

and CNT-MXene (below), excluding the edge Pt atoms. (b) Optimized geometric structures of Pt clusters on MXene (above) and CNT-MXene (below), where the green spheres represent the surface Pt atoms.

Conclusions

In summary, an integration of Pt metal and CNT-$Ti_3C_2T_x$ composite support through a facile chemical method is demonstrated in this work. The hybrid CNT-$Ti_3C_2T_x$ support has a strong influence on the electrocatalytic activity and stability of Pt catalyst. The mass activity and specific activity of Pt/CNT-$Ti_3C_2T_x$ (1:1) are 3.4 and 2.5 times than that of Pt/C, respectively. The superior ORR performance of Pt/CNT-$Ti_3C_2T_x$ (1:1) could be ascribed to the synergistic effect of its support individual components $Ti_3C_2T_x$ and CNT. The O_2 dissociation of Pt/CNT-$Ti_3C_2T_x$ (1:1) is much better than the Pt/C, and the desorption of O atom on composite catalyst become much easier when CNT added. Furthermore, the distortion of the Pt cluster could be reduced by introducing the CNT forward to Ti_3C_2Tx, which benefits to the catalytic stability. The Pt/CNT-$Ti_3C_2T_x$ (1:1) are used as cathode catalyst for PEMFC, and the maximum power density of fuel cell stack reach 138W.

Acknowledgements

Authors would thank the technical support for the fuel cell stack test from Kunshan Innovation Institute of Nanjing University. This work is supported by National Natural Science Foundation of China (21606064 and U1804130). The authors also

thank the Fundamental Research Funds for the Central Universities (JZ2018HGTB0252 and PA2018GDQT0021), the High Performance Computing Centre of Henan Normal University and the Engineering and Physical Sciences Research Council (EPSRC) grant number: EP/S032886/1.

Supporting Information Available: [Supporting Information include Roman spectra for Ti_3AlC_2 and $Ti_3C_2T_x$, XRD (Figure S1), XPS patterns (Figure S2, S3) for Pt/C and Pt/CNT-$Ti_3C_2T_x$, electrochemical test (Figure S4, S5) for Pt/CNT-$Ti_3C_2T_x$(1:1), Pt/CNT-$Ti_3C_2T_x$(1:2), Pt/CNT-$Ti_3C_2T_x$(2:1) and Pt/$Ti_3C_2T_x$, structure optimization of Pt/CNT-MXene and Pt/MXene cathodes (Figure S6), calculation of initial state, final state and dissociation energy barrier of oxygen dissociation process on Pt/MXene and Pt/CNT-MXene (Figure S7), PDOS results of Pt (111) surface, Pt/MXene (with and without carbon nanotubes) d electrons were calculated by the same number of Pt atoms (Figure S8), XPS curve fitting results of Pt/C and Pt/CNT- $Ti_3C_2T_x$ (1:1) catalysts (Table S1), ICP results of Pt content in Pt/C and Pt/ CNT- $Ti_3C_2T_x$ (1:1) catalysts (Table S2), E_{ad} of O_2, E_{bind} of O, and E_{dis} of O_2 on two kinds of Pt/C and Pt/CNT- $Ti_3C_2T_x$ (1:1) (Table S3).]

References:

1. Zhang, J.; Zhao, Y.; Guo, X. Single Platinum Atoms Immobilized on an MXene as an Efficient Catalyst for the Hydrogen Evolution Reaction. *Nature Catalysis* **2018**, *1*, 985.
2. Xie, X.; Chen, S.; Ding, W. An Extraordinarily Stable Catalyst: Pt NPs Supported on Two-Dimensional $Ti_3C_2X_2$ (X=OH, F) Nanosheets for Oxygen Reduction Reaction. *Chem. Commun.* **2013**, *49*, 10112-10114.

3. Xie, X.; Xue, Y.; Li, L. Surface Al leached Ti_3AlC_2 as a Substitute for Carbon for use as a Catalyst Support in a Harsh Corrosive Electrochemical System. *Nanoscale* **2014**, *6*, 11035-11040.
4. Wang, R.; Wang, H.; Luo, F.; Liao, S. Core–Shell-Structured Low-Platinum Electrocatalysts for Fuel Cell Applications. *Electrochem. Energ. Rev. CTAB* **2018**, *1*, 324-387.
5. Li, J.; Guan, Q.; Wu, H.; Liu, W.; Lin, Y.; Sun, Z.; Chen, S. Highly Active and Stable Metal Single-Atom Catalysts Achieved by Strong Electronic Metal–Support Interactions. *J. Am. Chem. Soc.* **2019**, *141*, 14515-14519.
6. Wei, M.; Jiang, M.; Liu, X.; Wang, M.; Mu, S. Graphene-Doped Electrospun Nanofiber Membrane Electrodes and Proton Exchange Membrane Fuel Cell Performance. *J. Power Sources* **2016**, *327*, 384-393.
7. Zhao, L.; Sui, X. L.; Li, J. L.; Zhang, J. J.; Zhang, L. M.; Wang, Z. B. 3D hierarchical Pt-Nitrogen-Doped-Graphene-Carbonized Commercially Available Sponge as a Superior Electrocatalyst for Low-Temperature Fuel Cells. *ACS Appl. Mater. Inter.* **2016**, *8*, 16026-16034.
8. Zhao, L.; Wang, Z. B.; Sui, X. L.; Yin, G. P. Effect of Multiwalled Carbon Nanotubes with Different Specific Surface Areas on the Stability of Supported Pt Catalysts. *J. Power Sources* **2014**, *245*, 637-643.
9. Cheng, K.; Zhu, K.; Liu, S.; Li, M.; Huang, J.; Yu, L.; Lu, W. A Spatially Confined gC_3N_4–Pt Electrocatalyst with Robust Stability. *ACS Appl. Mater. Inter.* **2018**, *10*, 21306-21312.
10. Bao, M.; Amiinu, I. S.; Peng, T.; Li, W.; Liu, S.; Wang, Z.; Mu, S. Surface Evolution of PtCu Alloy Shell over Pd Nanocrystals Leads to Superior Hydrogen Evolution and Oxygen Reduction Reactions. *ACS Energy Lett*. **2018**, *3*, 940-945.

11. Genorio, B.; Subbaraman, R.; Strmcnik, D. Tailoring the Selectivity and Stability of Chemically Modified Platinum Nanocatalysts to Design Highly Durable Anodes for PEM Fuel Cells. *Angew. Chem. Int. Edit.* **2011**, *50*, 5468-5472.
12. Sun, S.; Zhang, G.; Geng, D. A highly Durable Platinum Nanocatalyst for Proton Exchange Membrane Fuel Cells: Multiarmed Starlike Nanowire Single Crystal. *Angew. Chem. Int. Edit.* **2011**, *50*, 422-426.
13. Sui, X. L.; Li, C. Z.; Zhao, L.; Wang, Z. B.; Gu, D. M.; Huang, G. S. Mesoporous g-C_3N_4 Derived Nano-Titanium Nitride Modified Carbon Black as Ultra-Fine PtRu Catalyst Support for Methanol Electro-Oxidation. *Int. Hydrogen Energ.* **2018**, *43*, 5153-5162.
14. Li, M.; Zhao, Z.; Cheng, T. Ultrafine Jagged Platinum Nanowires Enable Ultrahigh Mass Activity for the Oxygen Reduction Reaction. *Science* **2016**, *354*, 1414.
15. Zhao, X.; Chen, S.; Fang, Z. Octahedral Pd@ $Pt_{1.8}Ni$ Core–Shell Nanocrystals with Ultrathin PtNi Alloy Shells as Active Catalysts for Oxygen Reduction Reaction. *J. Am. Chem. Soc.* **2015**, *137*, 2804.
16. Ma, Y.; Gao, W.; Shan, H. Platinum-Based Nanowires as Active Catalysts toward Oxygen Reduction Reaction: In Situ Observation of Surface-Diffusion-Assisted. *Adv. Mater.* **2017**, *29*, 1703460.
17. Sui, X. L.; Wang, Z. B.; Li, C. Z.; Zhang, J. J.; Zhao, L. Gu, D. M. Effect of Core/Shell Structured TiO_2@C Nanowire Support on the Pt Catalytic Performance for Methanol Electrooxidation. *Catal. Sci. Technol.* **2016**, *6*, 3767-3775.
18. Zhao, L.; Sui, X. L.; Li, J. Z.; Zhang, J. J.; Zhang, L. M.; Huang, G. S.; Wang, Z.

B. Supramolecular Assembly Promoted Synthesis of Three-Dimensional Nitrogen Doped Graphene Frameworks as Efficient Electrocatalyst for Oxygen Reduction Reaction and Methanol Electrooxidation. *Appl. Catal. B-Environ.* **2018**, *231*, 224-233.

19. Xia, B. Y.; Ng, W. T.; Wu, H. B. Self-Supported Interconnected Pt Nanoassemblies as Highly Stable Electrocatalysts for Low-Temperature Fuel Cells. *Angew. Chem. Int. Edit.* **2012**, *51*, 7213-7216.
20. Xia, Y.; Mathis, T. S.; Zhao, M. Q. Thickness-Independent Capacitance of Vertically Aligned Liquid-Crystalline MXenes. *Nature* **2018**, *557*, 409-412.
21. Anasori, B.; Lukatskaya, M. R.; Gogotsi, Y. 2D Metal Carbides and Nitrides (MXenes) for Energy Storage. *Nat. Rev. Mater.* **2017**, *2*, 16098.
22. Raccichini, R.; Varzi, A.; Passerini, S. The Role of Graphene for Electrochemical Energy Storage. *Nat. Mater.* **2015**, *14*, 271–279.
23. Li, Z.; Cui, Y.; Wu, Z. Reactive Metal–Support Interactions at Moderate Temperature in Two-Dimensional Niobium-Carbide-Supported Platinum Catalysts. *Nature Catalysis* **2018**, *1***,** 349.
24. He, D.; Tang, H.; Kou, Z.; Pan, M.; Sun, X.; Zhang, J.; Mu, S. Engineered Graphene Materials: Synthesis and Applications for Polymer Electrolyte Membrane Fuel Cells. *Adv. Mater.* **2017**, *29*, 1601741.
25. Kou, Z.; Meng, T.; Guo, B.; Amiinu, I. S.; Li, W.; Zhang, J.; Mu, S. A Generic Conversion Strategy: From 2D Metal Carbides (M_xC_y) to M-Self-Doped Graphene toward High-Efficiency Energy Applications. *Adv. Funct. Mater*. **2017**, *27*, 1604904.
26. Xiu, L.; Wang, Z.; Yu, M. Aggregation-Resistant 3D MXene-Based Architecture

as Efficient Bifunctional Electrocatalyst for Overall Water Splitting. *ACS Nano* **2018**, *12*, 8017-8028.

27. Zhao, S.; Zhang, H. B.; Luo, J. Q. Highly Electrically Conductive Three-Dimensional $Ti_3C_2T_x$ MXene/Reduced Graphene Oxide Hybrid Aerogels with Excellent Electromagnetic Interference Shielding Performances. *ACS Nano* **2018**, *12*, 11193-11202.
28. Naguib, M.; Mochalin, V. N.; Barsoum, M. W. 25th Anniversary Article: MXenes: a New Family of Two-Dimensional Materials. *Adv. Mater.* **2014**, *26*, 992-1005.
29. Ming, M.; Ren, Y.; Hu, M. Promoted Effect of Alkalization on the Catalytic Performance of Rh/alk-$Ti_3C_2X_2$ (XO, F) for the Hydrodechlorination of Chlorophenols in Base-Free Aqueous Medium. *Appl. Catal. B: Environ.* **2017**, *210*, 462-469.
30. Xie, X.; Zhao, M. Q.; Anasori, B. Porous Heterostructured MXene/Carbon Nanotube Composite Paper with High Volumetric Capacity for Sodium-Based Energy Storage Devices. *Nano Energy* **2016**, *26*, 513-523.
31. Alhabeb, M.; Maleski, K.; Anasori, B. Guidelines for Synthesis and Processing of Two-Dimensional Titanium Carbide ($Ti_3C_2T_x$ MXene). *Chem. Mater.* **2017**, *29*, 7633-7644.
32. Kresse, G.; Furthmüller, J. Efficient Iterative Schemes for Ab Initio Total-Energy Calculations using a Plane-Wave Basis Set. *Phys. Rev. B* **1996**, *54*, 11169.
33. Kresse, G.; Hafner, J. Ab Initio Molecular Dynamics for Liquid Metals. *Phys. Rev. B* **1993**, *47*, 558.
34. Perdew, J. P.; Ruzsinszky, A.; Csonka, G. I. Restoring the Density-Gradient

Expansion for Exchange in Solids and Surfaces. *Phys. Rev. Lett.* **2008**, *101*, 136406.

35. Blöchl, P. E. Projector Augmented-Wave Method. *Phys. Rev. B* **1994**, *50*, 17953-17979.
36. Grimme, S.; Antony, J.; Ehrlich, S. A Consistent and Accurate Ab Initio Parametrization of Density Functional Dispersion Correction (DFT-D) for the 94 Elements H-Pu. *J. Chem. Phys.* **2010**, *132*, 154104.
37. Henkelman, G.; Uberuaga, B. P.; Jónsson, H. A Climbing Image Nudged Elastic Band Method for Finding Saddle Points and Minimum Energy Paths. *J. Chem. Phys.* **2000**, *113*, 9901-9904.
38. Scheibe, B.; Tadyszak, K.; Jarek, M. Study on the Magnetic Properties of Differently Functionalized Multilayered $Ti_3C_2T_x$ MXenes and Ti-Al-C Carbides. *Appl. Surf. Sci.* **2019**, *479*, 216-224.
39. Li, J.; Yin, H. M.; Li, X. B. Surface Evolution of a Pt–Pd–Au Electrocatalyst for Stable Oxygen Reduction. *Nat. Energy* **2017**, *2*, 17111.
40. Bharti, A.; Cheruvally, G. Influence of Various Carbon Nano-Forms as Supports for Pt Catalyst on Proton Exchange Membrane Fuel Cell Performance. *J. Power Sources* **2017**, *360*, 196-205.
41. Wang, Y. C.; Lai, Y. J.; Song, L. S-Doping of an Fe/N/C ORR Catalyst for Polymer Electrolyte Membrane Fuel Cells with High Power Density. *Angew. Chem. Int. Edit.* **2015**, *54*, 9907-9910
42. Greeley, J.; Stephens, I. E. L.; Bondarenko, A. S. Alloys of Platinum and Early

Transition Metals as Oxygen Reduction Electrocatalysts. *Nat. chem.* **2009**, *1*, 552.

43. Shao, M.; Chang, Q.; Dodelet, J. P. Recent Advances in Electrocatalysts for Oxygen Reduction Reaction. *Chem. Rev.* **2016**, *116*, 3594-3657.
44. Li, R.; Li, H.; Liu, J. First Principles Study of O_2 Dissociation on Pt (111) Surface: Stepwise Mechanism. *Int. J. Quantum Chem.* **2016**, *116*, 908-914.